Enhanced performance of carbon dots and Mn_3O_4 composite by phosphate in peroxymonosulfate activation

Yongjian Zhu [a],[1], Zhipeng Quan [a],[1], Bolun Zhang [a], Junhui Zheng [a], Jie Wang [a], Xinxin Zhang [a], Chi Zhang [a], Tao Yang [b], Xin He [a], Songnan Qu [c], Yeqing Chen [a],[*], Ping Liang [a],[*]

[a] *School of Applied Physics and Materials, Wuyi University, Jiangmen, Guangdong Province, China*
[b] *Jiangmen Key Laboratory of Synthetic Chemistry and Cleaner Production, School of Environmental and Chemical Engineering, Wuyi University, Jiangmen, Guangdong Province, China*
[c] *Joint Key Laboratory of the Ministry of Education Institute of Applied Physics and Materials Engineering, University of Macau, Macao 999078, China*

ARTICLE INFO

ABSTRACT

A composite of nitrogen-doped carbon dots and Mn_3O_4 (CMO) was synthesized using a facile hydrothermal and precipitation method for peroxymonosulfate (PMS) activation. Surprisingly, high concentrations of $H_2PO_4^-$ (DP, above 20 mM) significantly enhanced the degradation efficiency of bisphenol A (BPA). The improvement was not attributed to the accelerated cleavage of PMS or pH variation. Instead, DP could directly form a complex with CMO, generating Mn(III)-DP with a high potential (0.64 V vs. SCE, 100 mM of DP). Simultaneously, it decreased the oxidative potential of BPA from 0.69 to 0.38 V vs. SCE. The degradation pathways of BPA differed in the CMO/PMS and CMO/DP systems. These findings inspire further exploration of carbon dots-based catalysts in persulfate activation and unveil the origin of enhanced performances by phosphate.

1. Introduction

Phenolic compounds, such as bisphenol A (BPA), have become widespread in various natural water bodies due to the rapid growth of the plastic industry, posing a significant threat to both human health and the environment [1]. It is known to possess endocrine disrupting properties and has been linked to various health concerns such as hormone imbalance, reproductive disorders, and developmental abnormalities. However, traditional methods for degrading organic pollutants, including adsorption, separation, and oxidation, face challenges such as high cost, secondary pollution, and limited effectiveness [2]. In recent years, peroxymonosulfate (PMS)-based advanced oxidation processes (AOPs) have gained attention as a promising method for removing refractory organic pollutants [3–7]. PMS, with its asymmetrical structure, can be activated by catalysts to generate reactive oxygen species (ROS) [3,8–13]. Carbon dots (CDs), a type of emerging zero-dimensional carbonaceous nanomaterial, have promising advantages in the catalytic reaction [14–18]: (i) high surface area and active sites: due to small size (<10 nm) and abundant surface functional groups, carbon dots typically possess a high surface area and numerous active sites (-C=O,

graphitic N, pyridinic N, C=C, etc.) for the adsorption of PMS, promoting its activation and subsequent generation of ROS. (ii) unique electronic properties: excellent electron-transfer ability and electrical conductivity render carbon dots a good catalyst due to crystalline sp^2 carbon and some nitrogen species like graphitic N and pyridinic N. (iii) superior functionalization ability and tunability: the characteristics of carbon dots, such as size, carbon core and surface functional groups, can be readily controlled and tuned during synthesis. Additionally, abundant functional groups (-OH, COOH, $-NH_2$, etc.) on the surface of carbon dots could coordinate with metal ions and further improve intra-electron transfer. These properties make it possible to tailor the properties of the carbon dots to meet specific catalytic requirements. Huang et al. successfully synthesized Mn doped carbon polymer dots (Mn-CPDs) and comprehensively studied the interaction between CPDs and Mn^{2+} ions. Between carbon networks, Mn^{2+} ions and oxygen-containing functionalities form Mn-O bonds and bridge the sp^2 domain of carbon nuclei, consequently accelerating the electron flow between adjacent sp^2 domains and enhancing the electron transport in Mn-CPDs, which showed excellent catalytic performance in activating hydrogen peroxide to degrade methylene blue and Rhodamine B [19]. It

is inspired that metal-modified carbon dots should be designed for PMS activation.

It is crucial to evaluate catalytic performance in real water matrices with coexisting anions. Phosphate, a typical species, is known to generally inhibit catalytic degradation by scavenging highly oxidative radicals or complexing with active sites, hindering the interaction between PMS and catalysts [20–23]. However, there are reports suggesting that phosphate can accelerate degradation in some PMS-based systems. For instance, Li et al. reported that the phosphate ($H_2PO_4^-$) could enhance the PMS decomposition in kaolinite/PMS system [24]. Duan et al. reported that coexisting $H_2PO_4^-$ facilitates the generation of ROS and decreases the bonding dissociation energy of organics, thereby boosting the degradation efficiency [25]. The influence and interaction mechanism of phosphate in the PMS-based systems require further study.

In this study, we synthesized a nitrogen-doped carbon dots and Mn_3O_4 composite (CMO) through the coordination between Mn^{2+} and carboxyl groups on CDs to activate PMS for BPA degradation. Surprisingly, the degradation process was remarkably accelerated by high concentrations of $H_2PO_4^-$ (above 20 mM). We discovered that the enhanced degradation did not result from the accelerated decomposition of PMS or changes in pH values but originated from the direct interaction between CMO and $H_2PO_4^-$. We delve into the degradation mechanism in the CMO/$H_2PO_4^-$/BPA system and investigate the active sites. This work presents easily-fabricated catalysts with excellent catalytic performance and provides new insights into phosphate-involved catalytic oxidation.

2. Materials and methods

2.1. Chemical

Citric acid monohydrate (CA, 99.5%), ethanolamine (ETA, AR), manganese chloride tetrahydrate (MnCl$_2$•4 H$_2$O, 99.9%), isopropanol (99.8%), urea (99.0%), ethylenediamine (EDA, AR), BPA (99.8%), PMS (98.0%), tert-butyl alcohol (TBA, 99.5%), anhydrous sodium sulfate (Na$_2$SO$_4$, 98%), humic acid (HA), sodium chloride (NaCl, 99.5%), sodium dihydrogen phosphate (NaH$_2$PO$_4$, DP, 99.0%), sodium phosphate dibasic (Na$_2$HPO$_4$, 99.0%), sodium phosphate (Na$_3$PO$_4$, 96.0%), sodium bicarbonate (NaHCO$_3$, 99.5%), methanol (99.8%), Mn$_3$O$_4$ (99.5%) and sodium hydroxide (NaOH, ≥98.0%) were purchased from Aladdin. 5,5-Dimethyl-1-pyrroline N-oxide (DMPO, ≥98.0%) was obtained from Sigma-Aldrich. Furfuryl alcohol (FFA, 98.0%), p-benzoquinone (PBQ, 97.0%) and 2,2,6,6,-tetramethyl-4-piperidinol (TMP, 99.0%) were purchased from Macklin. Hydrochloric acid (HCl, 36.0%) was bought from Guangzhou Chemical Reagent Factory. Phosphoric acid (H$_3$PO$_4$, 85.0%) was obtained from Tianjin Baishi Chemical Co. Ltd. All the chemicals were used directly without further purification.

2.2. Synthesis of materials

The CMO was synthesized as shown in Scheme 1. Initially, CDs were fabricated through a hydrothermal method at 180 °C for 15 h, using CA (3.22 mM) and ETA (59.4 mM) as precursors. The resulting CDs are decorated by C=O groups. Subsequently, 1 mmol of MnCl$_2$•4 H$_2$O was completely dissolved in 100 µL deionized (DI) water and mixed with the aforementioned CDs solution. During this process, Mn^{2+} coordinated with the carboxyl functionalities on the CDs and precipitated out. After filtration and drying, CMO was obtained. For comparison, CMO#2−5 were prepared using the same procedure as CMO but with different kinds or concentrations of precursors (Table S1). Specifically, CMO#2 and CMO#4 were derived from the same precursors as CMO but with different concentrations of ETA (39.6 and 9.9 mM for CMO#2 and CMO#4, respectively). CMO#3 and CMO#5 employed ethylenediamine (EDA, 59.4 mM) and urea (59.4 mM) as the nitrogen sources instead of ETA, respectively. Additionally, the CMO powders, after interaction with PMS and DP, were filtered and dried, and named CMO-R and CMO-DP, respectively.

2.3. Characterizations

The samples' phases and morphologies were characterized using powder X-ray diffraction (XRD, PANalytical X′ pert Pro) with Cu Kα radiation (λ = 1.5418 Å) and a field emission scanning electron microscope (FESEM, ZEISS Sigma 500), respectively. Microstructures were observed using transmission electron microscopy (TEM, FEI Talos F200X), high-resolution transmission electron microscopy (HRTEM), and selected area electron diffraction (SAED). X-ray photoelectron spectroscopy (XPS) was conducted on an ESCALAB250Xi (Thermo Scientific) spectrometer equipped with an X-ray source (hυ = 1486.6 eV, monochromatic Al Kα, 150 W). Raman spectroscopy (LabRAM HR Evolution) was employed to investigate the structures of the samples and the interaction between materials and PMS/DP. Fourier transform infrared spectroscopy (FT-IR) spectra of samples were obtained using a Vertex Perkin–Elmer 580BIR spectrophotometer (Bruker) with the KBr-pellet technique. UV–vis absorption spectra were obtained on a U-3310 UV–vis spectrophotometer (Hitachi), revealing the consumption of PMS and the intermediates generated during the reaction. Photoluminescence (PL) was measured using a Hitachi F-4600 fluorescence spectrophotometer equipped with a 150 W xenon lamp as the excitation
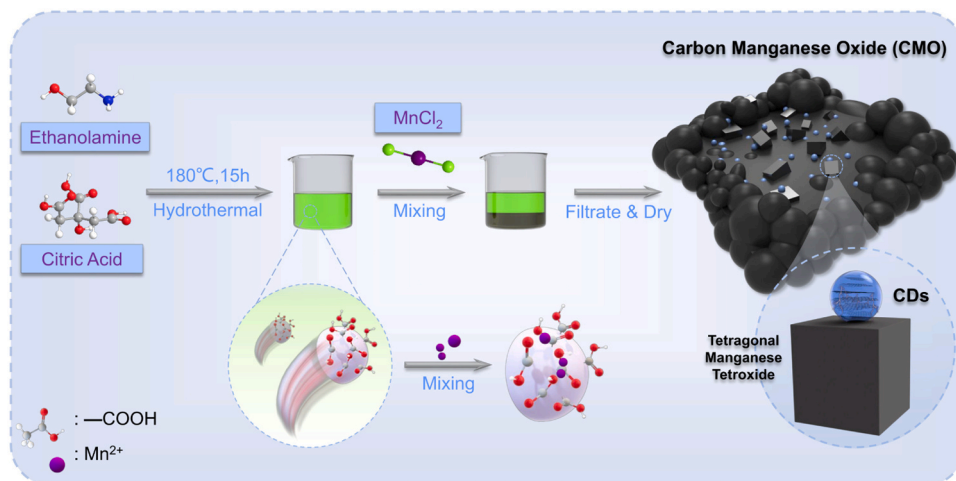
Scheme 1. The synthetic procedure of CMO.

source, verifying the existence of CDs and monitoring the decomposition of BPA.

2.4. Electrochemical tests

Electrochemical measurements, including cyclic voltammetry (CV), open circuit potential (OCP), and current-time (i-t) curves, were conducted to identify the interaction between CMO and PMS or DP. Detailed information is provided in **Text S1**.

2.5. Catalytic degradation procedures

Catalytic degradation experiments were conducted in a glass beaker containing a catalyst (0.1 g/L), PMS (3.25 mM), and the pollutant (10 ppm if not specified). At predetermined time intervals, a 1 mL solution was filtered through a 0.45 μm microporous membrane into a small vial containing 0.5 mL of methanol. The concentration of organic compounds was analyzed using a high-performance liquid chromatography system (HPLC, Waters e2695) equipped with a C-18 column. The mobile phases consisted of methanol and water, with a composition of 70:30 v/v for BPA and 45:55 v/v for phenol. The flow rate was set at 1 mL/min, and the detection wavelength was 254 (BPA) and 215 (phenol) nm. The initial pH of the solution was adjusted using hydrochloric acid and sodium hydroxide. Intermediates of BPA were identified by a mass spectrometer combined with HPLC (MS-HPLC, Thermo Fisher Scientific, Waltham, MA), and detailed parameters are provided in **Text S2**.

The generation of reactive oxygen species (ROS) was captured by an electron paramagnetic resonance instrument (EPR, Bruker EMXnano). DMPO was used as a spin-trapping reagent to distinguish sulfate radicals ($SO_4^{\bullet-}$), hydroxyl radicals ($\bullet OH$), and superoxide anions ($O_2^{\bullet-}$), while TMP was employed to trap singlet oxygen ($^1O_2$), forming 2,2,6,6-tetramethyl-4-piperidinol-N-oxyl (TMPN).

2.6. DFT calculation

Density functional theory (DFT) calculations were employed by the Vienna Ab Initio Simulation Package (VASP) software to determine the interaction between Mn_3O_4 and $H_2PO_4^-$, including the adsorption energy, charge density difference, density of states (DOS) and Bader charge, as described in **Text S3**.

3. Results and discussion

3.1. Morphology and structure

The morphology and structure of CMO are elucidated in Fig. 1. The SEM image (Fig. 1a) reveals irregular agglomerated particles of CMO. The TEM (Fig. 1b) and HRTEM (Fig. 1c-e) results demonstrate that the CMO comprises round carbon dots and tetragonal Mn_3O_4. The diffractions indexed to the (103), (211), and (321) planes of Mn_3O_4 are evident in the SAED patterns (inset of Fig. 1b). The d spacing of 0.236 nm determines the (103) plane of Mn_3O_4. The CDs are sized at ~3 nm, and an interplanar d spacing of ~0.21 nm is assigned to the (100) plane. The XRD result (Fig. 1f) confirms the phases of CMO. A broad peak at ~20° represents the lattice plane (002) of graphitic carbon in CDs [26], and peaks at 33° and 36° originate from the lattice plane (103) and (211) of Mn_3O_4, respectively. The Raman spectra of CMO in Fig. 1g correspond well with Mn_3O_4 [27]. The peaks of Mn(III)-O bending vibration (316 and 374 cm^{-1}) and Mn(II)-O stretching vibration (656 cm^{-1}) are noticeable in the Raman spectra [28]. Furthermore, an emission peak at 476 nm under excitation at 365 nm in the PL emission spectra (Fig. S1) of CMO verifies the existence of CDs within CMO. Conclusively, the CMO is the carbon dots and Mn_3O_4 composite.

3.2. The catalytic activity

The catalytic performance of catalysts in PMS activation for BPA removal was investigated. As shown in Fig. 2a, the degradation
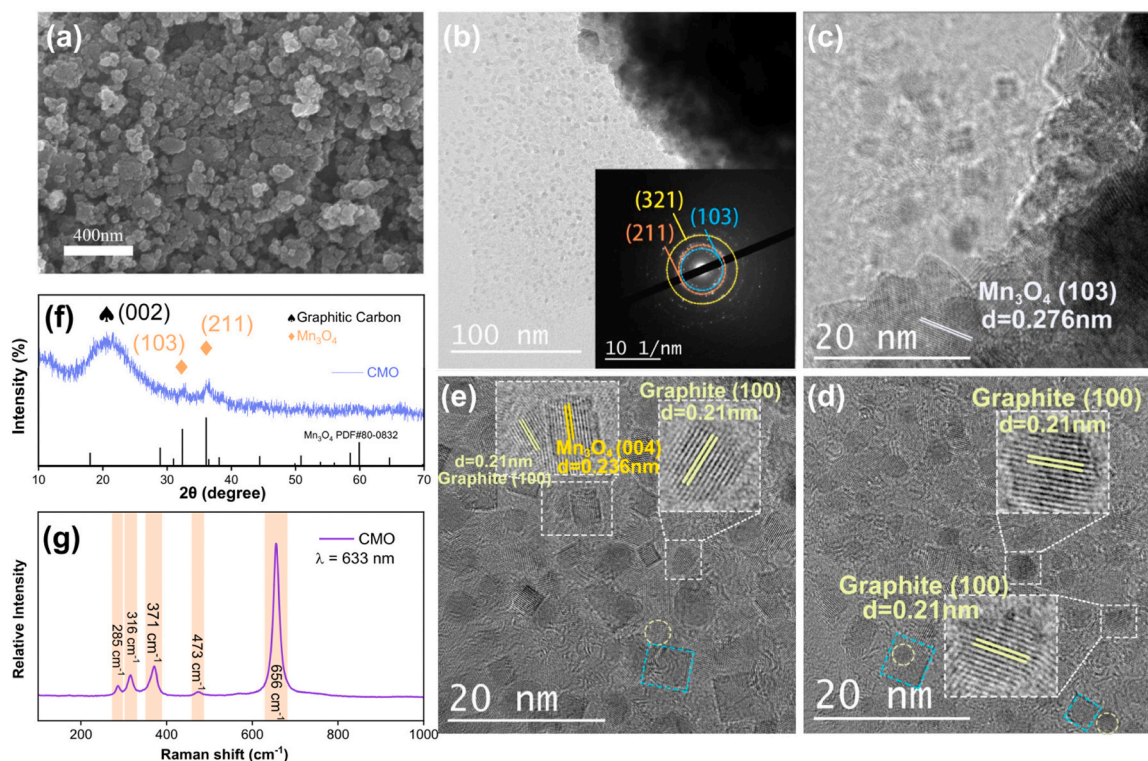

Fig. 1. (a) SEM, (b-c) TEMand (d-e) HR-TEM images of CMO, (f) XRD pattern and (g) Raman spectrum of CMO.
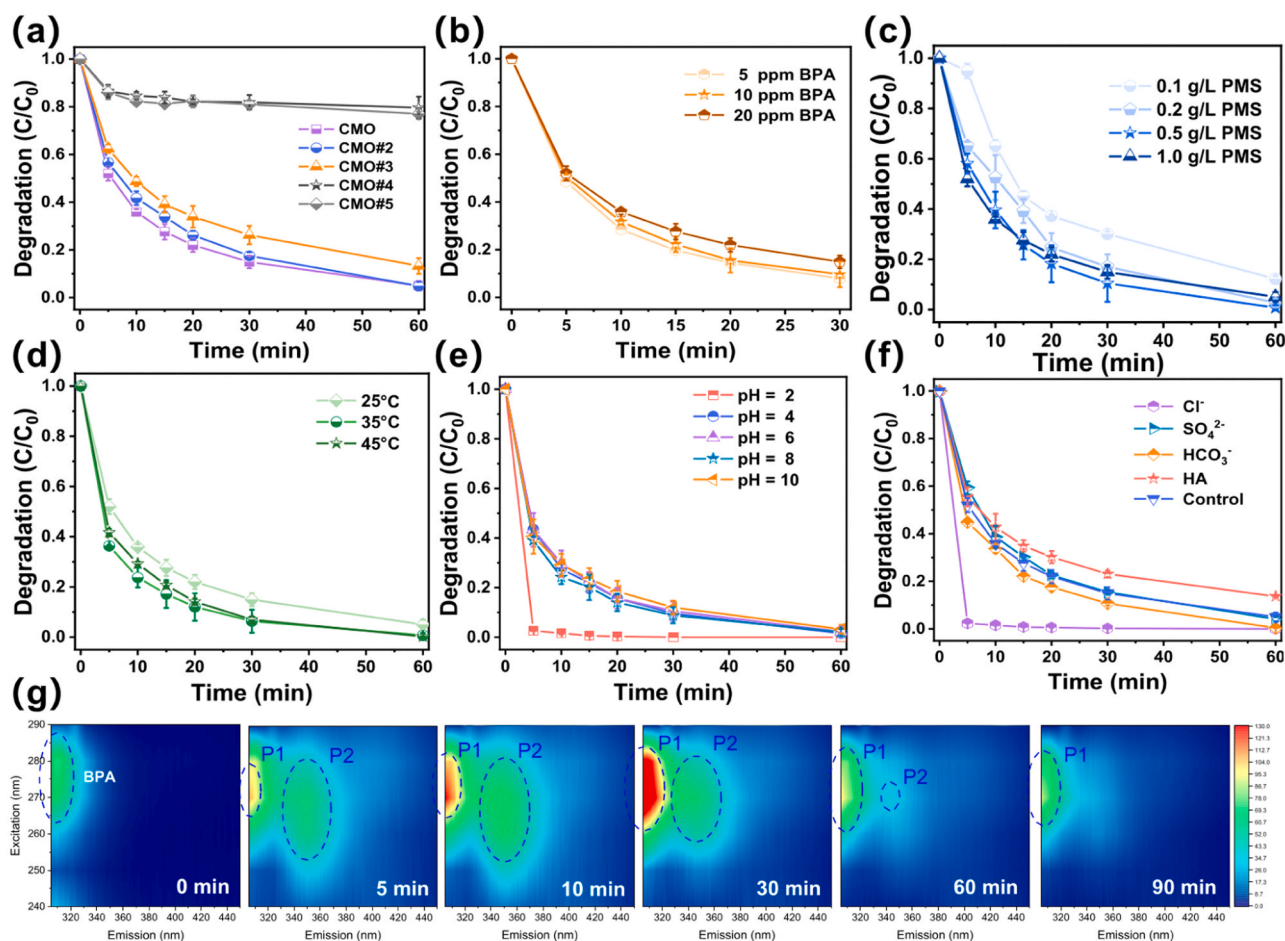
Fig. 2. (a) The catalytic performances of the as-synthesized materials, (b) the influence of BPA concentrations, (c) PMS dosages, (d) reaction temperatures, (e) initial pH values, and (f) the anions and HA on the catalytic activity of CMO, (g) the 2D EEM spectra of BPA at different reaction time. (Reaction conditions: $[SO_4^{2-}]_0 = [Cl^-]_0 = [HCO_3^-]_0 = [H_2PO_4^-]_0 = 10$ mM, $[HA]_0 = 10$ mg/L).

efficiency of BPA follows the sequence of CMO > CMO#2 > CMO#3 > CMO#4 ≈ CMO#5. CMO exhibits the highest catalytic activity, and BPA can be completely degraded in 60 minutes. The catalytic efficiencies of CMO#2 and CMO#3 are comparable to that of CMO, as they all consist of carbon and Mn_3O_4 (Fig. S2). However, only 20% of BPA could be removed by CMO#4 and CMO#5, as they contain $MnCO_3$ instead of Mn_3O_4 (Fig. S2).

The catalytic activity of CMO is not significantly affected by the initial BPA concentration (Fig. 2b), PMS dosage (Fig. 2c), and reaction temperature (Fig. 2d). Moreover, the catalytic degradation of BPA in the CMO/PMS system remains stable over a wide pH range of 4−10 (Fig. 2e). Remarkably, the degradation is significantly enhanced when the initial pH of the solution is adjusted to 2, and BPA can be completely eliminated in 5 min. To elucidate the role of an extremely acidic environment in degradation, the CMO/H_2SO_4 system without PMS was established, and the pH of the solution was adjusted to 2 (Fig. S3). It is observed that the degradation efficiency of BPA in the CMO/H_2SO_4 system is higher than that in the CMO/PMS system, indicating that CMO under extreme acidic conditions can directly oxidize BPA, and its oxidizing ability is superior to the CMO/PMS system. Previous reports have suggested that the protonation of high-valence manganese species under acidic conditions can attack organics via a direct oxidation process [29,30]. Inspired by this, the enhanced oxidizability of CMO at a pH value of 2 might be attributed to its protonation. Combining direct attack and catalytic oxidation, excellent degradation efficiency is achieved in the $CMO/PMS/H_2SO_4$ system.

Furthermore, the impact of wastewater matrix components, such as

inorganic anions and recalcitrant organic material (e.g., HA), on the catalytic performance of CMO is determined (Fig. 2f). Anions including SO_4^{2-} and HCO_3^- have a negligible influence on catalytic degradation, possibly due to the unfavorable adsorption of anions on the neutral surface of CMO (Fig. S4). Therefore, anions cannot interfere with the interaction between CMO and PMS. Although HA can consume the radicals such as $SO_4^{\bullet-}$ and •OH, the degradation shows no obvious suppression after adding HA, possibly due to that the free radicals are not responsible for the degradation in the CMO/PMS system. On the other hand, Cl^- dramatically accelerates the catalytic oxidation, requiring only 5 minutes to achieve complete removal of BPA, as the Cl^- can react with $SO_4^{\bullet-}$ and •OH to generate $Cl^{\bullet}$, which is more powerful in attacking BPA (Table S2) [31,32].

2D EEM (excitation emission matrix) spectra are used to visually monitor the decomposition of BPA (Fig. 2g). BPA can be observed at 310 nm. The signals assigned to the intermediates are found at 305 and 346 nm, and their intensities increase in the first 30 minutes, representing the degradation of BPA. Subsequently, the signals of intermediates weaken after 60 minutes of reaction, indicating further decomposition of the intermediates.

3.3. The effect of $H_2PO_4^-$ on catalytic performance

The catalytic activities of CMO after dosing DP with different concentrations are specifically studied (Fig. 3a), and the corresponding first-order reaction kinetic fitting (Fig. S5) and constants (k, Fig. 3b) are provided. Negligible degradation is found in the PMS/DP system,
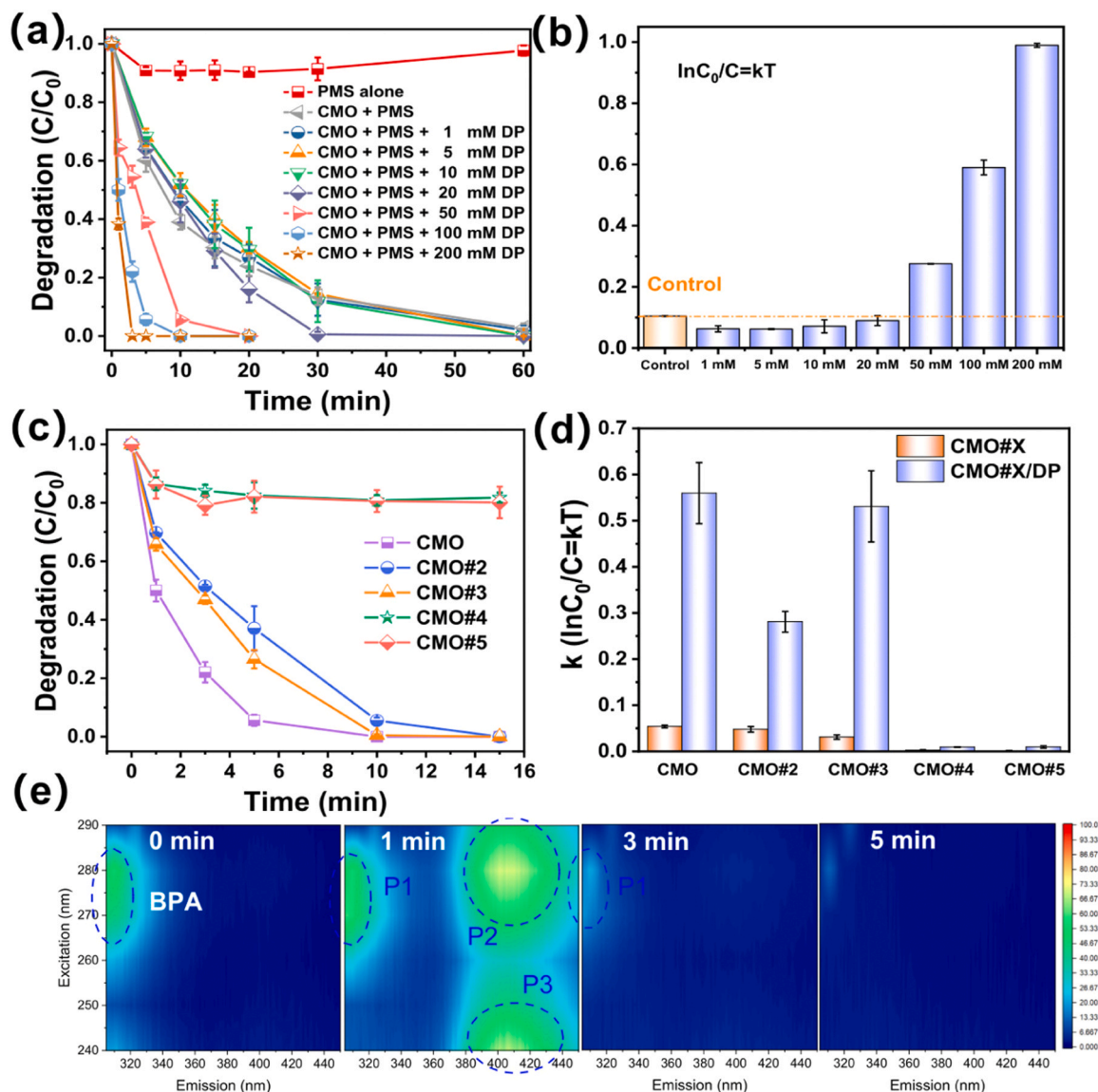
Fig. 3. (a) The influence of DP with different concentrations on catalytic degradation of CMO/PMS system and (b) the first-order reaction kinetics, (c) the influence of 100 mM DP on catalytic performances of different catalysts and (d) the first-order reaction kinetic constants, (e) the 2D EEM spectra of CMO/PMS/DP system at 100 mM DP concentration. (Reaction conditions: [catalysts]$_0$ = 0.1 g/L, [PMS]$_0$ = 1.0 g/L, [BPA]$_0$ = 10 ppm, T = 25 °C).

suggesting that DP cannot promote the cleavage of PMS. Low concentrations of DP, such as 1, 5, 10, and 20 mM, could inhibit degradation compared to the CMO/PMS system without DP in the solution. The negative effect of DP is possibly attributed to the following reasons: firstly, DP can quench $SO_4^{\bullet-}$ and $\bullet OH$ to produce $\bullet H_2PO_4^-$ or $\bullet HPO_4^-$ with lower potentials; secondly, DP can chelate with the metal sites in the catalysts, hindering the interaction between PMS and the active sites [33,34]. However, when the concentration of DP is raised above 20 mM, the degradation is promoted, and the efficiency becomes higher with the increase of DP concentrations. It takes 20, 10, and 3 min to completely remove BPA at concentrations of 50, 100, and 200 mM, respectively. Correspondingly, the k values increase from 0.104 (CMO/PMS system) to 0.995 min^{-1} (CMO/PMS/200 mM DP system). In addition, the half-time lives ($t_{1/2}$) are summarized in Table S3, and the oxidation ability is quantified by the ratio (r_{ligand}) of $t_{1/2}$ in the absence of DP to that of its counterparts with DP involved. The r_{ligand} values below 1.0 in the systems with low concentrations ($\leq$ 20 mM) of DP indicate that DP suppresses the oxidation, while above 1.0 with high concentrations ($\geq$ 50 mM) of DP represents the promoted oxidation by DP.

Moreover, we investigated the influence of DP in different catalysts/

PMS systems (Figs. 3c, d and S6). It is found that catalysts containing MnCO$_3$ have no response to the addition of DP, while the degradation of BPA is greatly improved by DP for CMO#2 and CMO#3, which have similar phases to CMO. The k values of CMO#2/PMS/DP and CMO#3/PMS/DP are 17.15 and 6.08 times those of CMO#2/PMS and CMO#3/PMS system, respectively. Therefore, it can be concluded that high concentrations of DP accelerate the catalytic degradation of BPA in the CMO/PMS system, possibly due to the existence of Mn$_3$O$_4$. The 2D EEM spectra (Fig. 3e) reveal the degradation of BPA in the CMO/PMS/DP system, in which it can be seen that the intermediates are generated after 1 min and diminished after 3 min. The EEM spectra here could also prove the promotion of degradation efficiency by high concentrations of DP, compared to the spectra in Fig. 2g. In addition, the intermediate spectra in the CMO/PMS/DP system are different from those in the CMO/PMS system, suggesting that the degradation pathway of BPA might be modified after the addition of DP. Noteworthily, the HCO$_3^-$ does not influence the catalytic effect (Fig. S7). It is necessary to figure out the mechanism in the CMO/PMS/DP system.

3.4. The promotion mechanism of $H_2PO_4^-$

3.4.1. The effect on PMS activation by $H_2PO_4^-$

It was previously reported that the phosphate, such as PO_4^{3-} and HPO_4^{2-} could boost the cleavage of O-O in PMS, thereby promoting the generation of $SO_4^{\bullet-}$ [35]. Inspired by it, the degradation efficiencies of BPA are tested with various concentrations of PMS by adding DP (Fig. 4a), and the result shows that no obvious removal can be obtained. In addition, as the EPR spectra (Fig. 4b) reveal, no obvious peaks can be observed in the DP/PMS system, suggesting that DP could not activate PMS. Meanwhile, the DMPO could not trap any radicals from DP alone. CMO alone could not generate reactive radicals when being mixed with DMPO, but the typical signal assigned to DMPO-OH adduct ($\alpha_N = 14.8$ G, $\alpha_N = 14.8$ G) can be found in the CMO/PMS system (Fig. 4b and S8), indicating the activation of PMS by CMO. When DP was added to the CMO/PMS system, the intensity of peaks is significantly suppressed (Fig. 4a and S9), which is similar to the EPR signal generated by PMS alone.

As shown in Fig. 4c, the characteristic signal of TMPN ($\alpha_N = 16.9$ G) in the CMO/PMS system is greatly intensified compared to PMS alone, indicating that $^1O_2$ is produced during PMS activation. However, when DP was added, the signal of TMPN could hardly be observed, similar to the phenomenon trapping by DMPO above. It can be concluded that $\bullet$OH and $^1O_2$ can be generated during the activation of PMS by CMO, and DP would induce the annihilation of the oxidative species. The findings above exclude the possibility that the promotion of DP on the degradation is induced by the faster breaking of O-O in PMS.

Quenching tests were conducted to verify the effect of ROS on the degradation of BPA. The reaction rates of typical quenchers are provided in Table S4. Methanol was utilized as a scavenger of $\bullet$OH and $SO_4^{\bullet-}$, and TBA as the quencher of $\bullet$OH. As shown in Fig. S10, both methanol and TBA exert negligible influence on the efficiency in the CMO/PMS system, representing that the as-generated free radicals like $\bullet$OH and $SO_4^{\bullet-}$ contribute little to the degradation. Furthermore, when FFA and PBQ, as a $^1O_2$ and $O_2^{\bullet-}$ scavenger respectively, were added in the CMO/PMS system, the degradation efficiency can be well maintained, suggesting that $^1O_2$ and $O_2^{\bullet-}$ are also not the main reasons for the dissociation of BPA. Similarly, ROS, including $\bullet$OH, $SO_4^{\bullet-}$ and $^1O_2$ exert no effect on the efficiency of the CMO/PMS/DP system (Fig. 4d). The PBQ seems to decrease the degradation limitedly, possibly due to the generation of some reactive oxygen. Nowack *et al.* previously reported that O_2-Mn(II)-phosphate complex could be formed in the presence of manganese, dissolved molecular oxygen, and phosphate [36]. Subsequently, the O_2 can be activated *via* intramolecular electron transfer. In this work, the degradation becomes slower when the reaction solution is treated by nitrogen purging while is boosted by purging oxygen in the solution (Fig. S11), suggesting that the dissolved oxygen takes effect on the degradation through the above route, and the reactive oxygen originates from the O_2. Based on the analysis above, it is further confirmed that the improved performance after the participation of DP is not caused by the boosted cleavage of PMS and increased concentrations of ROS.

3.4.2. The effect of pH variation by $H_2PO_4^-$

The pH variation during the reaction should be considered, as the protonation of manganese species can oxidize the organics directly under acidic conditions [37]. We monitored the pH values of BPA/DP
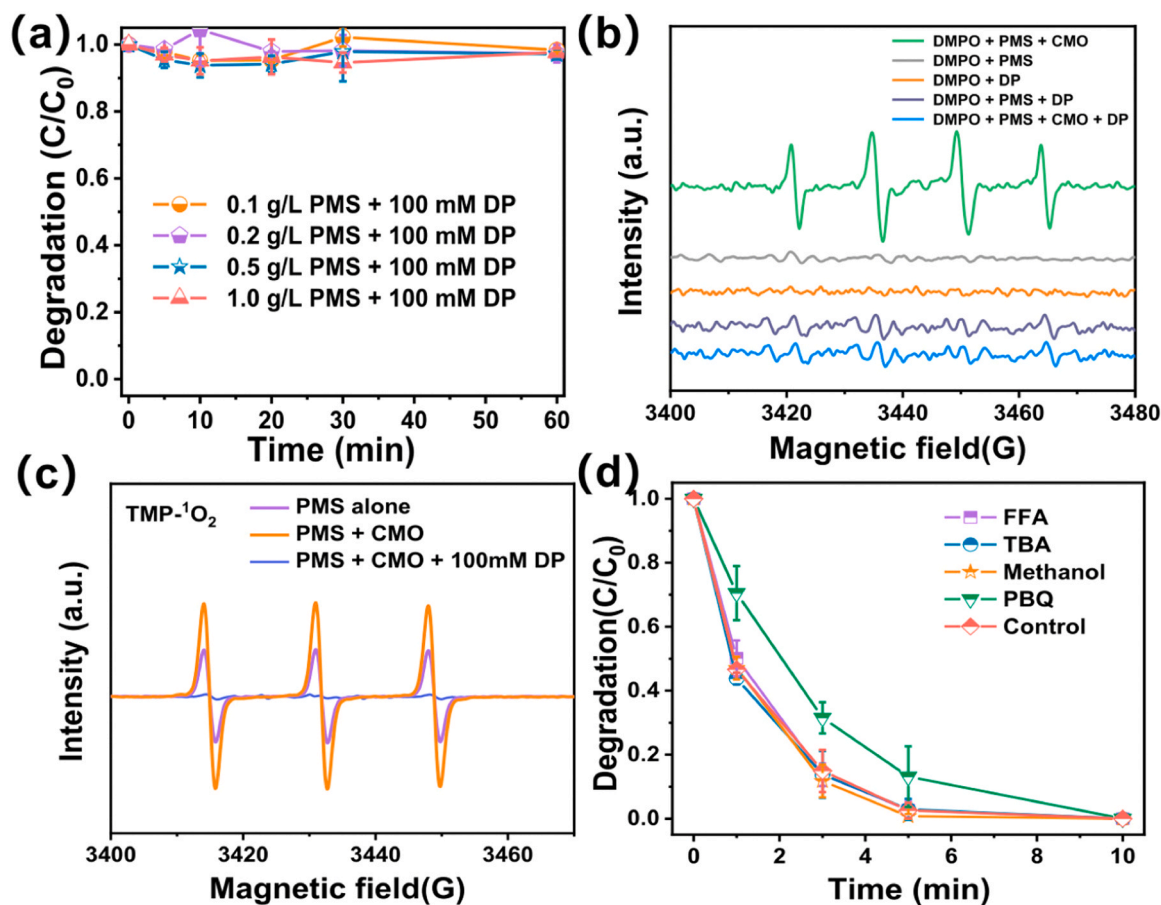

Fig. 4. (a) The degradation efficiency in the PMS/DP systems, (b) DMPO and (c) TMP spin-trapping EPR spectra in the systems, (d) effects of scavengers on the catalytic efficiency of CMO/PMS/DP system. (Reaction conditions: [catalysts] = 0.1 g/L, [PMS] = 3.25 mM, [BPA] =10 ppm, [DP] = 100 mM, [Methanol] = [TBA] = 650 mM, [PBQ] = [FFA] = 10 mM).

and BPA/DP/CMO systems, which are maintained at ~4.6 (Fig. 5a). After adding PMS, the pH value decreases and stays around 4.0 during the reaction. So, the H_2SO_4 was dropped in the CMO/BPA solution to adjust the pH values to 4.6 and 4.0 (Fig. 5b). It is observed that CMO alone has little adsorption ability on BPA, and the decomposition of BPA at pH values of 4.6 and 4.0 is similar to the adsorption, which is significantly slower than that in the CMO+PMS+100 mM DP+BPA system. The findings above suggest that the improved degradation efficiency induced by DP is not attributed to the pH variation and protonation of CMO.

3.4.3. The reaction between CMO and $H_2PO_4^-$

The variation of PMS concentrations in the CMO/PMS and CMO/PMS/100 mM DP systems during the reaction is examined to investigate the interaction between CMO and DP (Fig. 5c). About 20% of PMS is consumed by CMO, but negligible PMS decomposition is monitored after the participation of DP. We propose that CMO prefer to complex with DP rather than PMS, and the excellent performance in the CMO/PMS/DP system might be attributed to the interaction between CMO and DP.

The CMO/DP systems are established to verify the assumption above (Fig. 5d). CMO/DP could degrade BPA without PMS in the system, and the efficiency is improved with the increase of DP concentrations. The pseudo-first-order rate constant is deduced (Fig. 5e and S12), and the n_{ligand} values of the CMO/DP systems are also calculated (Fig. 5f and Table S3). It can be seen that the degradation in the CMO/DP system with low DP concentrations (not more than 20 mM) is slower than that in the corresponding CMO/PMS/DP and CMO/PMS systems, suggesting that the oxidation ability of the CMO/DP system is weaker than that of the CMO/PMS system, and the DP could hinder the interaction between CMO and PMS. When the concentration of DP arrives at 100 mM, CMO/DP has a similar degradation efficiency to CMO/PMS/DP because enough DP has replaced PMS ultimately to interact with CMO. The degradation efficiency of phenol by the CMO/DP system is evaluated in Fig. S13. About 90% of phenol could be decomposed in 20 min, suggesting the powerful oxidizing ability of the CMO/DP system. Based on the analysis above, it can be concluded that the promoted oxidative efficiency by high concentrations of DP is originated from the direct interaction between CMO and DP. We investigated the influence of
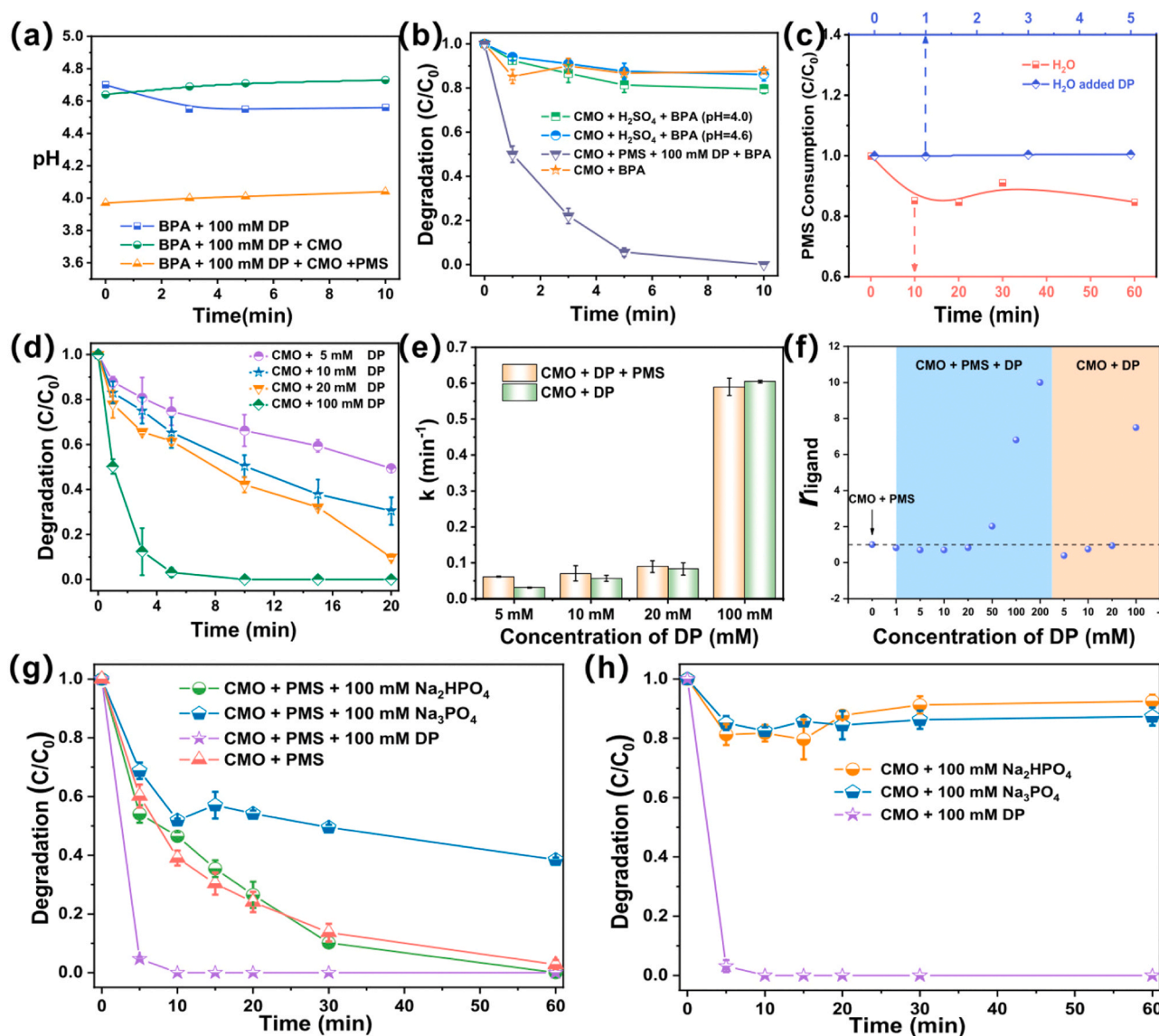

Fig. 5. (a) The pH variation after adding DP, (b) removal efficiency of BPA at initial pH values of 4.0 and 4.6 mediated by H_2SO_4, (c) the PMS consumption by CMO and CMO/DP, (d) the degradation efficiency of BPA in the CMO/DP system without PMS, (e) the comparison of reaction rates between CMO/DP/PMS and CMO/DP systems, (f) the n_{ligand} values of different reaction systems, (g) the effect of HPO_4^{2-} and PO_4^{3-} on the CMO/PMS system, (h) the degradation efficiency in the CMO/HPO_4^{2-} and CMO/PO_4^{3-} systems.

reaction temperatures (Fig. S14a) and typical coexisting anions/HA (Fig. S14b) on the degradation performance of CMO/DP system. The degradation efficiency could be improved by higher reaction temperatures. The anions Cl^- and SO_4^{2-} could slightly inhibit the degradation of BPA, because they may repel the adsorption of $H_2PO_4^-$ on the Mn site of CMO. The organic substance HA also inhibit the reaction, possibly due to its competitive consumption of Mn(III)-DP complex. The degradation of BPA is significantly inhibited by the addition of HCO_3^-, resulting from the complexation of HCO_3^- with Mn site in the CMO which induces the occupation of the active sites, and thus inhibiting the reaction.

We also tested the influence of other phosphate species, like HPO_4^{2-} and PO_4^{3-}, on the catalytic effect of CMO/PMS system (Fig. 5g). It shows that the HPO_4^{2-} and PO_4^{3-} cannot promote the efficiency or even hinder the degradation. Moreover, the degradation by CMO/HPO_4^{2-} and CMO/PO_4^{3-} systems without PMS is also identified (Fig. 5h), revealing that negligible removal of BPA is observed, which is significantly different from the CMO/DP system. Moreover, the degradation of BPA in the CMO/H_3PO_4 system is studied (Fig. S15a), showing that 80% of BPA could be decomposed in 10 min. As the solution is extremely acidic (pH

= 2, Fig. S15b) after adding H_3PO_4, the removal of BPA might be induced by the protonation of high-valence manganese species as the influence of H_2SO_4 in Fig. S3. We are inspired to explore the oxidative mechanism of the CMO/DP system.

3.4.4. The reaction mechanism between CMO and $H_2PO_4^-$

No distinct EPR signals of free radicals are trapped by DMPO in the CMO/DP system (Fig. S16). Combined with the quenching effect as-mentioned above, nonradical pathways should be considered. The CV curves (Fig. 6a) for the BPA and BPA + DP solutions demonstrate that the oxidation potential (E_p) of BPA decreases from 0.69 V to 0.38 V vs. SCE after adding DP in the electrolyte, indicating that the DP makes BPA easier to be decomposed. The OCP value (Fig. 6b) of CMO is measured to be ~0.45 V, which is lower than the E_p (0.69 V) of BPA, which could explain why CMO cannot alone oxidize BPA in Fig. 5b. When 100 mM of DP is added in the electrolyte, the OCP rises to 0.64 V. It is also found that the OCP increases with the concentrations of DP (Fig. S17), which is 0.59, 0.61, 0.63 V for 5, 10, and 20 mM of DP, respectively. The potentials are greater than the E_p (0.38 V) of BPA, indicating that the
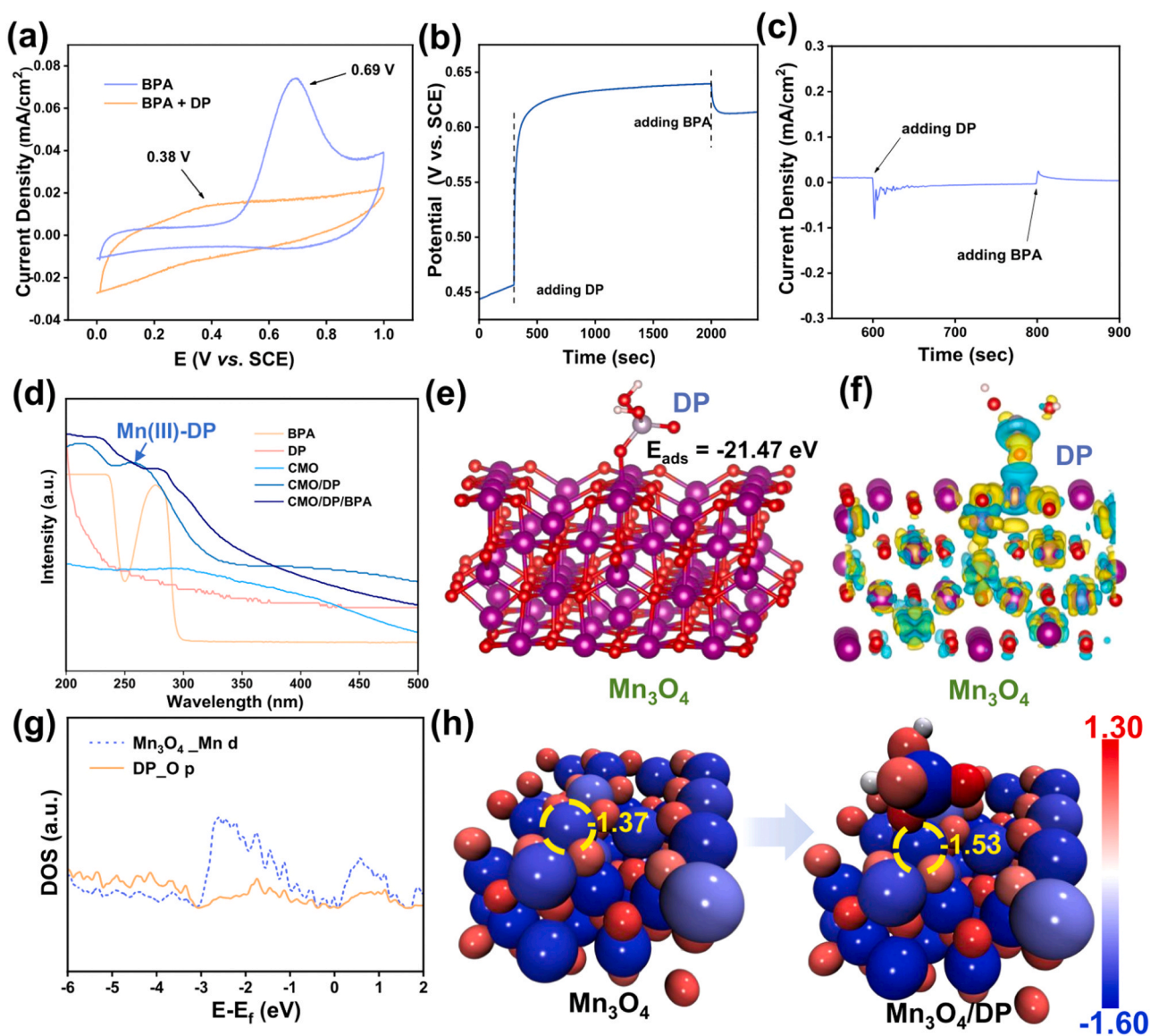

Fig. 6. (a) CV curves of BPA, (b) OCP and (c) i-t curves of CMO+DP system, (d) UV–vis spectra of BPA, DP, CMO, CMO/DP and CMO/DP/BPA system, (e) the adsorption of DP on Mn_3O_4, (f) charge density difference on Mn_3O_4 and DP (The yellow and blue denote the electron accumulation and electron depletion, respectively.), (g) the DOS of Mn d in Mn_3O_4 and O p in DP after adsorption, (h) the Bader charges of Mn in Mn_3O_4 before (left) and after (right) DP adsorption.

CMO/DP system owns the ability to oxidize BPA. When BPA is added in the electrolyte, the potential drops due to the electrons transferred from BPA to the electrode. The i-t curve (Fig. 6c) reveals the electron transfer during the catalytic reaction. The reduction current after adding DP suggests that electrons are transferred from CMO to DP. The oxidation current initiated by the participation of BPA is assigned to the electrons transferred from BPA to the CMO/DP system.

The UV–vis spectra (Fig. 6d) record the interaction between CMO and DP. Compared with the spectra of DP and CMO, an additional absorbance peak at ~260 nm appears in the CMO/DP system spectrum. It was previously reported that sodium pyrophosphate (PP) could bond with Mn(III) to form a reactive intermediate, which owns the characteristic UV–vis absorbance peak at ~258 nm [38]. Inspired by it, we propose that the peak at ~260 nm in this work is assigned to the formation of Mn(III)-DP complex. When BPA is added in the solution, the Mn(III)-DP complex signal is undetectable, possibly due to the electron transfer from BPA to the complex during oxidation. No peak of Mn (III)-based complex can be found in the UV–vis spectra of CMO/HCO_3^-, CMO/HPO_4^{2-}, CMO/H_3PO_4 and CMO/PO_4^{3-} systems (Fig. S18), which is consistent with the above degradation results in Fig. 5h and S7, and further confirms the oxidative ability of CMO/H_3PO_4 (Fig. S15) is originated from the extreme acidic environment. In addition, we tested the oxidative ability of Mn_3O_4/DP system (Fig. S19), showing that the sole Mn_3O_4 could complex with DP to degrade BPA efficiently. The DFT calculations were conducted to observe the interaction between DP (Fig. S20a) and Mn_3O_4 (Fig. S20b) further. As shown in Fig. 6e, the DP tends to be adsorbed on the Mn site of Mn_3O_4, and the adsorption energy is –21.47 eV. The charge density difference in Fig. 6f certifies that noticeable electron transfer exists between DP and Mn_3O_4, corresponding to the above electrochemical and UV–vis results. Correspondingly, the DOS overlap between Mn d in Mn_3O_4 and O p in DP

reveals the interaction between the Mn site in Mn_3O_4 and O site in DP (Fig. 6g). The Bader charge in Mn_3O_4 is more negative after DP adsorption (Fig. 6h), which is decreased to –1.53 from –1.37, indicating that the Mn site donates more electrons. Conclusively, the mechanism in the CMO/DP system is that the Mn(III)-DP complex is formed by the chemisorption of DP on Mn_3O_4, which could directly oxidize BPA. Although the promotion effect of DP in the PMS-based advanced oxidation has been studied previously as we mentioned above, the intrinsic mechanism is considered to be the enhanced PMS decomposition, more generation of ROS or the decreased bonding dissociation energy of organics. In this work, we propose a new pathway: the catalyst could bond with DP directly without the participation of PMS.

3.5. Active sites

XPS investigates the surface chemical states of CMO, CMO-R and CMO-DP to elucidate the active sites. According to XPS survey spectra in Fig. 7a, the peaks of C 1 s, O 1 s, N1s, and Mn 2p could be observed in CMO, CMO-R and CMO-DP. Noteworthily, an additional peak at around 135 eV in the spectrum of CMO-DP is attributed to P 2p originating from DP. The high-resolution XPS spectra of Mn 2p (Fig. 7b) have a $2p_{3/2}$– $2p_{1/2}$ doublet at 642.1 and 653.7 eV, and the splitting width is 11.6 eV, representing the formation of Mn_3O_4 [39]. The multiple splitting widths (ΔE) of Mn 3 s (Fig. 7c) could reveal the average oxidation state (AOS) of Mn. The ΔE values of CMO, CMO-R, and CMO-DP are 5.3, 5.1, and 5.0 eV, respectively. According to the equation, AOS = 8.95 – 1.13ΔE, the AOS of Mn in CMO-R and CMO-DP is higher than that in CMO. In the CMO/PMS system, the Mn(II) could be oxidized into Mn(III) by PMS to generate free radicals including •OH and $SO_4^{\bullet-}$. In addition, the as-generated Mn(III) could further donate electrons to PMS *via* redox reaction or complexation, forming Mn(IV) [40]. Therefore, the valence
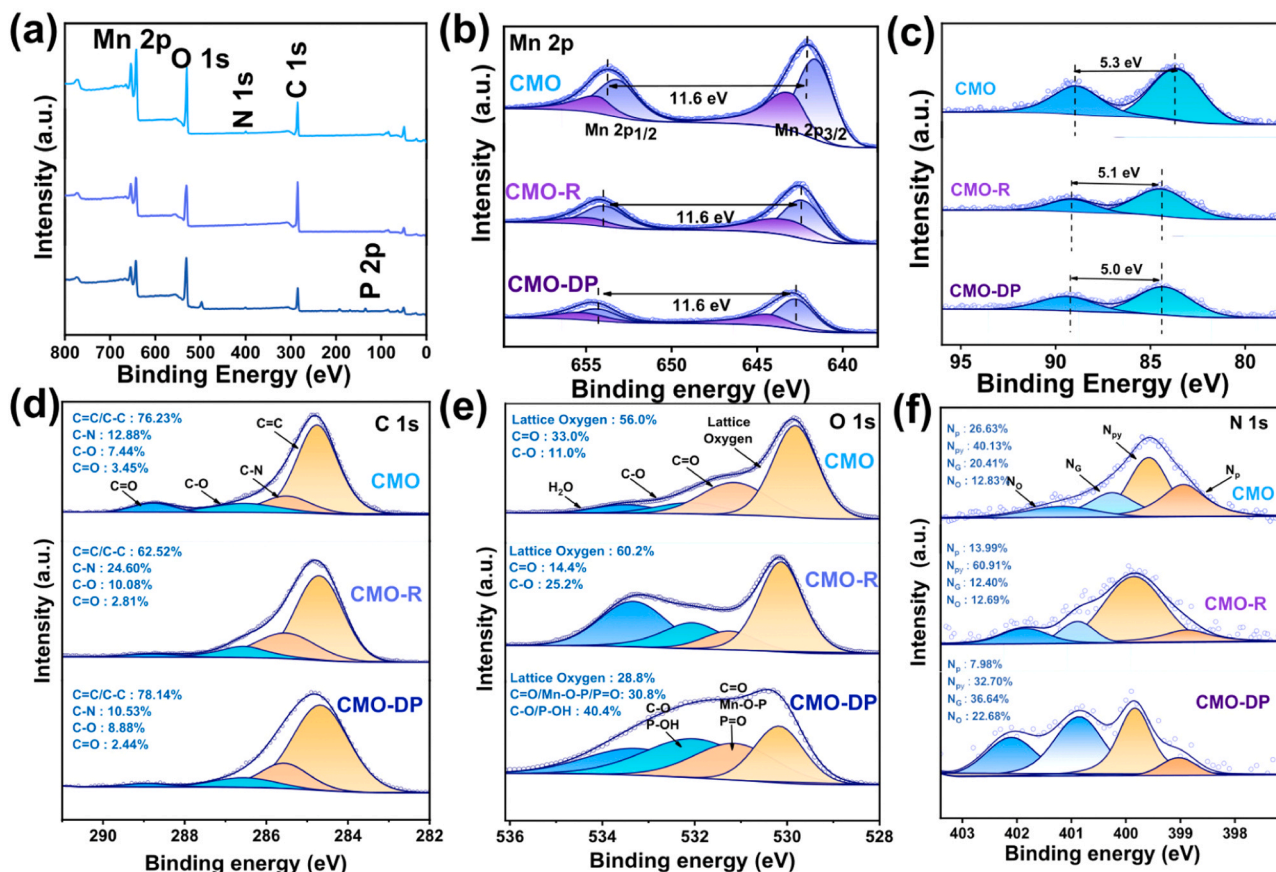

Fig. 7. (a) The XPS survey spectra, the high-resolution XPS spectra of (b) Mn 2p, (c) Mn 3 s, (d) C 1 s, (e) O 1 s and (f) N 1 s in CMO, CMO-R and CMO-DP.

state of Mn in CMO-R increases compared to CMO. In the CMO/DP system, the electrons are transferred from the Mn site to DP during the formation of the Mn(III)-DP complex, as discussed above, which induces the AOS rise of Mn in CMO-DP.

The high-resolution XPS spectra of C 1 s (Fig. 7d) can be deconvoluted into four peaks, corresponding to C=C (284.8 eV), C-N (285.4 eV), C-O (286.7 eV), and C=O (288.7 eV) [41–44]. It was previously reported that the C=C and C=O could interact with PMS to generate ●OH, $SO_4^{\bullet-}$ and $^1O_2$ [45,46]. In this work, the contents of C=C and C=O in CMO-R (62.52% and 2.81%, respectively) are less than CMO (76.23% and 3.45%, respectively), indicating that the two components in CMO participate in the PMS activation to produce ROS as evidenced by the EPR spectra mentioned above (Figs. 4b and c). In CMO-DP, no obvious change can be found in the content of C=C compared to CMO, but the amount of C=O decreases. As previously reported [47], the OH group in DP could consume the C=O by nucleophilic attack. Therefore, the percentage of C=O in CMO-DP decreases. Meanwhile, the high-resolution XPS spectra of O 1 s (Fig. 7e) are deconvoluted into four components, including lattice oxygen (530.0 eV), C=O (531.1 eV), C-O (532.0 eV) and H_2O (533.3 eV). The lattice oxygen in CMO-R (60.2%) is more than CMO (56.0%), corresponding to the valence state increase of Mn. In addition, the CMO-R (14.4%) contains less C=O than CMO (33.0%), which is consistent with the XPS results of C 1 s. Noteworthily, the lattice oxygen in CMO-DP (28.8%) is greatly less than CMO, which contradicts its larger valence state of Mn. As mentioned above, the DP could be complex with CMO, and P peak is observed in the XPS survey spectrum of CMO-DP. In addition, the peaks at 531.1 and 532.0 eV can also be attributed to Mn-O-P/P=O and P-OH, respectively [48]. Therefore, the decrease of lattice oxygen is induced by the participation of P-based groups. The existence of Mn-O-P here reconfirms the formation of the Mn(III)-DP complex. In addition, the emission properties of CDs in CMO indeed can be maintained after reaction in CMO/PMS and CMO/DP systems (Fig. S21), revealing that CDs exhibit good stability during the catalytic degradation.

As the doped N in carbon is generally considered the active site in the catalytic reaction [49], the N-bonding configurations in CMO, CMO-R, and CMO-DP are investigated. In the high-resolution XPS spectra of N 1 s (Fig. 7f), four peaks at 398.9, 399.6, 400.3, and 401.4 eV are attributed to pyridinic N (N_p), pyrrolic N (N_{py}), graphitic N (N_G) and oxidized N (N_O), respectively. The proportion of graphitic N in CMO-R is lower than that in CMO, indicating that the graphitic N acts as the active site in the CMO/PMS system. It has been reported that graphitic N with strong electronegativity could attract electrons from the adjacent carbon, which is induced to be positively charged and mediates the formation of $^1O_2$ by nucleophilic reaction of the PMS molecules [50]. In addition, the graphitic N also facilitates the formation of metastable PMS, which owns weak O-O and decomposes the electron-rich organics directly [51]. The addition of PMS can improve the OCP (Fig. S22a) of CMO, and apparent reduction current (Fig. S22b) is achieved correspondingly. Based on the analysis above, the phenomenon is induced by the reaction between Mn(III)/Mn(II) redox cycle and PMS and the interaction between C=C/C=O/graphitic N and PMS. The OCP decreases after the participation of BPA, and oxidation current appears, suggesting that the BPA is oxidized. Due to the negligible effect of ROS on the degradation, as elucidated in Fig. S10, the BPA in the CMO/PMS system is directly decomposed by the metastable PMS. Compared with CMO, the proportions of pyridinic N and pyrrolic N in CMO-DP are significantly decreased. As previously reported [52], the DP could poison the pyridinic/pyrrolic N sites in the carbon through the formation of inactive pyridinic-NH/ pyrrolic-NH species and blocking the positively charged neighboring C atoms of pyridinic/pyrrolic N. Inspired by it, the N-doped carbon in CMO cannot take effect in the CMO/DP system, and consequently, the Mn_3O_4 in CMO is the sole active site.

Based on the analysis above, the mechanism in this work is summarized (Fig. 8) as below: in the CMO/PMS system, the Mn(III)/Mn(II) redox cycle and C=C/C=O/graphitic N in the carbon dots react with PMS to generate ROS, such as ●OH, $SO_4^{\bullet-}$ and $^1O_2$, which have negligible effect on the BPA degradation; meanwhile, the graphitic N would trigger the formation of metastable PMS, which attack the organic *via* direct electron transfer. In the CMO/DP system, the pyridinic/pyrrolic N and C=O are poisoned by DP, which become inactive; the Mn(III)-DP complex is formed and degrades BPA through a nonradical pathway; in addition, the intramolecular electron transfer in the O_2-Mn(II)-DP complex could produce $O_2^{\bullet-}$, which would decompose BPA.

3.6. Degradation pathway

As mentioned in the EEM results, the BPA might be degraded *via* different pathways in the CMO/PMS and CMO/DP systems. The intermediates are identified (Fig. S23), and the degradation pathway is established in Fig. 9. Once the reaction is initiated, the BPA first endures the β-scission (C-C) and is then transformed into intermediates through Route I and II. Noteworthily, the BPA in the CMO/PMS system is degraded via Route I, while BPA in the CMO/DP system is decomposed through both Route I and Route II. In Route I, the intermediates contain 1-(4-methyl phenyl) ethenone (m/z = 135.08), p-(α-Hydroxyethyl)
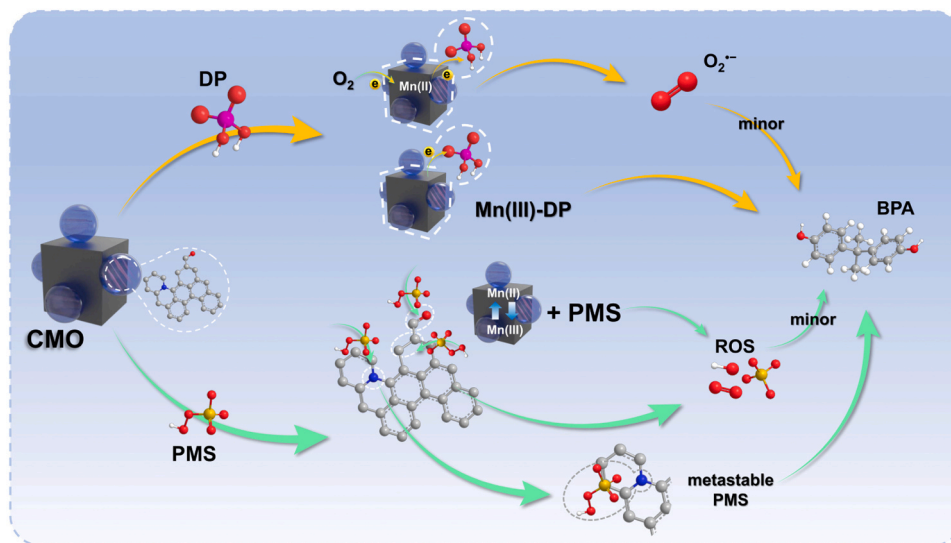

Fig. 8. The mechanism of the CMO/PMS and CMO/DP systems.
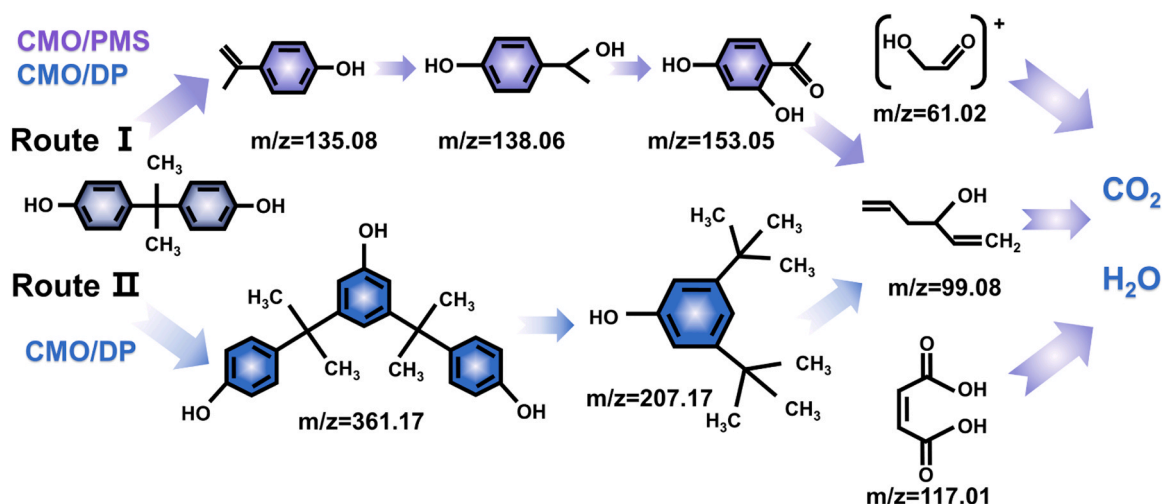
Fig. 9. The degradation pathway of BPA in the CMO/PMS and CMO/DP systems.

phenol ($m/z = 138.06$) and 1-(2,4-dihydroxyphenyl) ethenone ($m/z = 153.05$). In Route II, the intermediates including 4,4'-((4-hydroxyl-1,3-phenylene)bis(propane-2,2-diyl))diphenol ($m/z = 361.17$) and Phenol,3,5-bis(1,1-dimethyl(ethyl)) ($m/z = 207.17$) are observed. During the reaction, the intermediates are transformed *via* hydroxylation, dehydration, oxidative skeletal rearrangement, *etc*. The aromatic rings in the intermediates are attacked and opened finally, forming CO_2 and H_2O.

4. Conclusions

The composite material (CMO), consisting of nitrogen-doped carbon dots and Mn_3O_4, is synthesized through a facile hydrothermal method. It demonstrates excellent catalytic performance in PMS activation for BPA degradation. The graphitic nitrogen-doped in the carbon matrix reacts with PMS, forming metastable PMS, which degrades BPA via a non-radical pathway. High concentrations (> 20 mM) of DP are found to promote the efficiency of the CMO/PMS system significantly. DP preferentially chelates with CMO in the CMO/PMS/DP system, and a high concentration of DP completely hinders the interaction between CMO and PMS. The CMO/DP system without PMS can degrade BPA, improving efficiency with increased DP concentrations. The pyridinic nitrogen and adjacent carbon are transformed into inactive sites due to the poisoning effect of DP. Mn_3O_4, as the sole active site, chelates with DP to form highly oxidative Mn(III)-DP, which directly decomposes BPA. Meanwhile, the oxidative potential of BPA decreases after the addition of DP. Moreover, dissolved O_2 can be activated into $O_2^{\bullet-}$ through electron transfer in the O_2-Mn(II)-DP complex, attacking BPA through a radical pathway. BPA in the CMO/PMS and CMO/DP systems is degraded through different pathways. The study provides a new insight into the promotion mechanism of phosphates in persulfate-based oxidation. It is significant for the exploration of highly effective catalysts and provides inspiration for understanding the mechanism of advanced oxidation.

Declaration of Competing Interest

The authors declare that they have no known competing financial interests or personal relationships that could have appeared to influence the work reported in this paper.

Data availability

Data will be made available on request.

Acknowledgments

Appendix A. Supporting information

Supplementary data associated with this article can be found in the online version at doi:10.1016/j.apcatb.2024.123954.

References

[1] J. Gao, J. Song, J. Ye, X. Duan, D.D. Dionysiou, J.S. Yadav, M.N. Nadagouda, L. Yang, S. Luo, Comparative toxicity reduction potential of UV/sodium percarbonate and UV/hydrogen peroxide treatments for bisphenol A in water: an integrated analysis using chemical, computational, biological, and metabolomic approaches, Water Res. 190 (2021) 116755.

[2] C.C. Wang, J.R. Li, X.L. Lv, Y.Q. Zhang, G. Guo, Photocatalytic organic pollutants degradation in metal–organic frameworks, Energ. Environ. Sci. 7 (2014) 2831–2867.

[3] Q. Yang, X. Niu, Y. Zhu, Y. Cui, Y. Chao, P. Liang, C. Zhang, S. Wang, Modulating anion defect in $La_{0.6}Sr_{0.4}Co_{0.8}Fe_{0.2}O_{3-\delta}$ for enhanced catalytic performance on peroxymonosulfate activation: importance of hydrated electrons and metal-oxygen covalency, J. Hazard. Mater. 432 (2022) 128686.

[4] P. Duan, J. Pan, W. Du, Q. Yue, B. Gao, X. Xu, Activation of peroxymonosulfate via mediated electron transfer mechanism on single-atom Fe catalyst for effective organic pollutants removal, Appl. Catal. B-Environ. 299 (2021) 120714.

[5] P. Li, Y. Lin, S. Zhao, Y. Fu, W. Li, R. Chen, S. Tian, Defect-engineered Co_3O_4 with porous multishelled hollow architecture enables boosted advanced oxidation processes, Appl. Catal. B-Environ. 298 (2021) 120596.

[6] S. Liu, Z. Zhang, F. Huang, Y. Liu, L. Feng, J. Jiang, L. Zhang, F. Qi, C. Liu, Carbonized polyaniline activated peroxymonosulfate (PMS) for phenol degradation: role of PMS adsorption and singlet oxygen generation, Appl. Catal. B-Environ. 286 (2021) 119921.

[7] X. Zhao, X. Li, Z. Zhu, W. Hu, H. Zhang, J. Xu, X. Hu, Y. Zhou, M. Xu, H. Zhang, Single-atom Co embedded in BCN matrix to achieve 100% conversion of peroxymonosulfate into singlet oxygen, Appl. Catal. B-Environ. 300 (2022) 120759.

[8] J. Lee, U. Von Gunten, J.-H. Kim, Persulfate-based advanced oxidation: critical assessment of opportunities and roadblocks, Environ. Sci. Technol. 54 (2020) 3064–3081.

[9] L. Peng, X. Duan, Y. Shang, B. Gao, X. Xu, Engineered carbon supported single iron atom sites and iron clusters from Fe-rich Enteromorpha for Fenton-like reactions via nonradical pathways, Appl. Catal. B-Environ. 287 (2021) 119963.

[10] L. Peng, Y. Shang, B. Gao, X. Xu, Co_3O_4 anchored in N, S heteroatom co-doped porous carbons for degradation of organic contaminant: role of pyridinic N-Co binding and high tolerance of chloride, Appl. Catal. B-Environ. 282 (2021) 119484.

[11] Y. Shang, X. Xu, B. Gao, S. Wang, X. Duan, Single-atom catalysis in advanced oxidation processes for environmental remediation, Chem. Soc. Rev. 50 (2021) 5281–5322.

[12] S. Yanan, X. Xing, Q. Yue, B. Gao, Y. Li, Nitrogen-doped carbon nanotubes encapsulating Fe/Zn nanoparticles as a persulfate activator for sulfamethoxazole degradation: role of encapsulated bimetallic nanoparticles and nonradical reaction, Environ. Sci. Nano 7 (2020) 1444–1453.

[13] S. Yang, S. Xu, J. Tong, D. Ding, G. Wang, R. Chen, P. Jin, X.C. Wang, Overlooked role of nitrogen dopant in carbon catalysts for peroxymonosulfate activation: intrinsic defects or extrinsic defects? Appl. Catal. B-Environ. 295 (2021) 120291.

[14] H. Xu, N. Jiang, D. Wang, L. Wang, Y. Song, Z. Chen, J. Ma, T. Zhang, Improving PMS oxidation of organic pollutants by single cobalt atom catalyst through hybrid radical and non-radical pathways, Appl. Catal. B-Environ. 263 (2020) 118350.

[15] W. Li, Y. Liu, M. Wu, X. Feng, S.A. Redfern, Y. Shang, X. Yong, T. Feng, K. Wu, Z. Liu, Carbon-quantum-dots-loaded ruthenium nanoparticles as an efficient electrocatalyst for hydrogen production in alkaline media, Adv. Mater. 30 (2018) 1800676.

[16] Z. Zhu, K. Ge, Z. Li, J. Hu, P. Chen, H. Bi, Nickel-doped carbon dots as an efficient and stable electrocatalyst for urea oxidation, Small 19 (2023) 2205234.

[17] S.A. Rub Pakkath, S.S. Chetty, P. Selvarasu, A. Vadivel Murugan, Y. Kumar, L. Periyasamy, M. Santhakumar, S.R. Sadras, K. Santhakumar, Transition metal ion (Mn^{2+}, Fe^{2+}, Co^{2+}, and Ni^{2+})-doped carbon dots synthesized via microwave-assisted pyrolysis: a potential nanoprobe for magneto-fluorescent dual-modality bioimaging, ACS Biomater. Sci. Eng. 4 (2018) 2582–2596.

[18] S. Tao, T. Feng, C. Zheng, S. Zhu, B. Yang, Carbonized polymer dots: a brand new perspective to recognize luminescent carbon-based nanomaterials, J. Phys. Chem. Lett. 10 (2019) 5182–5188.

[19] J. Huang, Y. Chen, P. Rao, X. Ni, X. Chen, J. Zhu, C. Li, G. Xiong, P. Liang, X. He, Enhancing the electron transport, quantum yield, and catalytic performance of carbonized polymer dots via Mn-O bridges, Small 18 (2022) 2106863.

[20] P. Duan, T. Ma, Y. Yue, Y. Li, X. Zhang, Y. Shang, B. Gao, Q. Zhang, Q. Yue, X. Xu, Fe/Mn nanoparticles encapsulated in nitrogen-doped carbon nanotubes as a peroxymonosulfate activator for acetamiprid degradation, Environ. Sci. Nano 6 (2019) 1799–1811.

[21] G.-X. Huang, C.-Y. Wang, C.-W. Yang, P.-C. Guo, H.-Q. Yu, Degradation of bisphenol A by peroxymonosulfate catalytically activated with $Mn_{1.8}Fe_{1.2}O_4$ nanospheres: synergism between Mn and Fe, Environ. Sci. Technol. 51 (2017) 12611–12618.

[22] N. Li, Y. Wang, X. Cheng, H. Dai, B. Yan, G. Chen, S. Wang, Influences and mechanisms of phosphate ions onto persulfate activation and organic degradation in water treatment: a review, Water Res. 222 (2022) 118896.

[23] Z. Liu, H. Ding, C. Zhao, T. Wang, P. Wang, D.D. Dionysiou, Electrochemical activation of peroxymonosulfate with ACF cathode: kinetics, influencing factors, mechanism, and application potential, Water Res. 159 (2019) 111–121.

[24] C. Li, Y. Huang, X. Dong, Z. Sun, X. Duan, B. Ren, S. Zheng, D.D. Dionysiou, Highly efficient activation of peroxymonosulfate by natural negatively-charged kaolinite with abundant hydroxyl groups for the degradation of atrazine, Appl. Catal. B-Environ. 247 (2019) 10–23.

[25] P. Duan, Y. Qi, S. Feng, X. Peng, W. Wang, Y. Yue, Y. Shang, Y. Li, B. Gao, X. Xu, Enhanced degradation of clothianidin in peroxymonosulfate/catalyst system via core-shell FeMn@NC and phosphate surrounding, Appl. Catal. B-Environ. 267 (2020) 118717.

[26] H. Song, Y. Cheng, B. Li, Y. Fan, B. Liu, Z. Tang, S. Lu, Carbon dots and RuP₂ nanohybrid as an efficient bifunctional catalyst for electrochemical hydrogen evolution reaction and hydrolysis of ammonia borane, ACS Sustain. Chem. Eng. 8 (2020) 3995–4002.

[27] J.E. Post, D.A. McKeown, P.J. Heaney, Raman spectroscopy study of manganese oxides: tunnel structures, Am. Miner. 105 (2020) 1175–1190.

[28] H. Liu, X. Dai, L. Kong, C. Sui, Z. Nie, Y. Liu, B. Cai, S.-Q. Ni, G. Boczkaj, J. Zhan, Ball milling treatment of Mn₃O₄ regulates electron transfer pathway for peroxymonosulfate activation, Chem. Eng. J. 467 (2023) 143339.

[29] S. Balgooyen, P.J. Alaimo, C.K. Remucal, M. Ginder-Vogel, Structural transformation of MnO₂ during the oxidation of bisphenol A, Environ. Sci. Technol. 51 (2017) 6053–6062.

[30] N. Shaikh, S. Taujale, H. Zhang, K. Artyushkova, A.-M.S. Ali, J.M. Cerrato, Spectroscopic investigation of interfacial interaction of manganese oxide with triclosan, aniline, and phenol, Environ. Sci. Technol. 50 (2016) 10978–10987.

[31] C.-H. Liao, S.-F. Kang, F.-A. Wu, Hydroxyl radical scavenging role of chloride and bicarbonate ions in the H_2O_2/UV process, Chemosphere 44 (2001) 1193–1200.

[32] G.-D. Fang, D.D. Dionysiou, Y. Wang, S.R. Al-Abed, D.-M. Zhou, Sulfate radical-based degradation of polychlorinated biphenyls: effects of chloride ion and reaction kinetics, J. Hazard. Mater. 227 (2012) 394–401.

[33] Y. Xu, H. Lin, Y. Li, H. Zhang, The mechanism and efficiency of MnO₂ activated persulfate process coupled with electrolysis, Sci. Total Environ. 609 (2017) 644–654.

[34] Y. Xu, J. Ai, H. Zhang, The mechanism of degradation of bisphenol A using the magnetically separable CuFe₂O₄/peroxymonosulfate heterogeneous oxidation process, J. Hazard. Mater. 309 (2016) 87–96.

[35] P. Duan, X. Liu, B. Liu, M. Akram, Y. Li, J. Pan, Q. Yue, B. Gao, X. Xu, Effect of phosphate on peroxymonosulfate activation: accelerating generation of sulfate radical and underlying mechanism, Appl. Catal. B-Environ. 298 (2021) 120532.

[36] B. Nowack, A.T. Stone, Degradation of nitrilotris (methylenephosphonic acid) and related (amino) phosphonate chelating agents in the presence of manganese and molecular oxygen, Environ. Sci. Technol. 34 (2000) 4759–4765.

[37] Y. Yang, P. Zhang, K. Hu, X. Duan, S. Wang, Sustainable redox processes induced by peroxymonosulfate and metal doping on amorphous manganese dioxide for nonradical degradation of water contaminants, Appl. Catal. B-Environ. 286 (2021) 119903.

[38] B. Sun, X. Guan, J. Fang, P.G. Tratnyek, Activation of manganese oxidants with bisulfite for enhanced oxidation of organic contaminants: the involvement of Mn (III), Environ. Sci. Technol. 49 (2015) 12414–12421.

[39] Y. Liu, J. Luo, L. Tang, C. Feng, J. Wang, Y. Deng, H. Liu, J. Yu, H. Feng, J. Wang, Origin of the enhanced reusability and electron transfer of the carbon-coated Mn₃O₄ nanocube for persulfate activation, ACS Catal. 10 (2020) 14857–14870.

[40] S. Shen, L. He, Y. Ma, L. Yang, X. Zhou, Q. Zhao, W. Jiang, J. Wang, Z. Chen, Understanding the nonradical activation of peroxymonosulfate by different crystallographic MnO₂: the pivotal role of Mn^{III} content on the surface, J. Hazard. Mater. 439 (2022) 129613.

[41] J. Chen, C.F. Wang, Y. Zhang, S. Yang, S. Chen, Metal ions doped carbon dots with strongly yellow photoluminescence, Rsc Adv. 6 (2016) 37189–37194.

[42] M. Le, B. Hu, M. Wu, H. Guo, L. Wang, Construction of Co,N-coordinated carbon dots for efficient oxygen reduction reaction, Molecules 27 (2022) 5021.

[43] Q. Peng, Q. Zhou, Antioxidant capacity of flavonoid in soybean seedlings under the joint actions of rare earth element La(III) and ultraviolet-B stress, Biol. Trace Elem. Res. 132 (2009) 270–277.

[44] Z. Zhu, X. Li, M. Luo, M. Chen, W. Chen, P. Yang, X. Zhou, Synthesis of carbon dots with high photocatalytic reactivity by tailoring heteroatom doping, J. Colloid Interf. Sci. 605 (2022) 330–341.

[45] S. Liu, Z. Zhang, F. Huang, Y. Liu, C. Liu, Carbonized polyaniline activated peroxymonosulfate (PMS) for phenol degradation: role of PMS adsorption and singlet oxygen generation, Appl. Catal. B-Environ. 286 (2021) 119921.

[46] Q. Wang, Y. Jiang, X. Lin, H. Li, Z. Wang, W. Wang, Insight into novel Fe₃C/ Mo₂C@carbonized polyaniline activated PMS for parachlorophenol degradation: key roles of Mo^{2+}, C═O bonds and N-doping, Sep. Purif. Technol. 322 (2023) 124359.

[47] A. Zare, N. Lotfifar, M. Dianat, Preparation, characterization and application of nano-[Fe₃O₄@-SiO₂@R-NHMe₂][H₂PO₄] as a novel magnetically recoverable catalyst for the synthesis of pyrimido[4,5-b]quinolines, J. Mol. Struct. 1211 (2020) 128030.

[48] W. Jiang, Z. Qiu, W. Yao, Y. Zhu, W. Cui, TiO₂/Al(H₂PO₄)₃ composite film as separation-free and washing-resistance photocatalyst, Appl. Catal. B-Environ. 204 (2017) 43–48.

[49] P. Liang, Q. Wang, J. Kang, W. Tian, H. Sun, S. Wang, Dual-metal zeolitic imidazolate frameworks and their derived nanoporous carbons for multiple environmental and electrochemical applications, Chem. Eng. J. 351 (2018) 641–649.

[50] S. Wang, L. Xu, J. Wang, Nitrogen-doped graphene as peroxymonosulfate activator and electron transfer mediator for the enhanced degradation of sulfamethoxazole, Chem. Eng. J. 375 (2019) 122041.

[51] S. Ye, G. Zeng, X. Tan, H. Wu, J. Liang, B. Song, N. Tang, P. Zhang, Y. Yang, Q. Chen, Nitrogen-doped biochar fiber with graphitization from Boehmeria nivea for promoted peroxymonosulfate activation and non-radical degradation pathways with enhancing electron transfer, Appl. Catal. B-Environ. 269 (2020) 118850.

[52] K. Mamtani, D. Jain, D. Zemlyanov, G. Celik, J. Luthman, G. Renkes, A.C. Co, U. S. Ozkan, Probing the oxygen reduction reaction active sites over nitrogen-doped carbon nanostructures (CNx) in acidic media using phosphate anion, ACS Catal. 6 (2016) 7249–7259.